Numerical analysis of high temperature minichannel heat exchanger for recuperative microturbine system

Jan Wajs [a, *], Tomasz Kura [b], Dariusz Mikielewicz [a], Elzbieta Fornalik-Wajs [b], Jarosław Mikielewicz [c]

[a] *Gdansk University of Technology, Faculty of Mechanical Engineering and Ship Technology, Poland*
[b] *AGH University of Science and Technology, Faculty of Energy and Fuels, Poland*
[c] *Institute of Fluid-Flow Machinery, Centre of Heat and Power Engineering, Poland*

ARTICLE INFO

ABSTRACT

Considering the development of energy sector, distributed small-scale power generation, e.g., gas micro-CHP, is attracting considerable interest. In such installations, the heat exchanger is one of the key components possessing a significant influence on overall performance. Most studies concentrate on units operating below 900 °C, which do not fulfil the requirements of gas micro-CHP. Therefore, there remains a challenge to design a compact heat exchanger with passive technologies of heat transfer enhancement. This work describes the implementation of the own construction of a plate minichannel heat exchanger for high-efficiency gas microturbine engines with an external combustion chamber, supplied with air at a temperature of about 1000 °C. The results of this study will greatly contribute to the increase of system efficiency. To understand transport phenomena occurring inside it, a numerical model of the entire heat exchanger was developed in OpenFOAM. Defined boundary conditions were based on experimental data used also to validate the numerical model. The pressure drop experimental and numerical results agreed within the 2%–14% range, while the heat rate ones – within the 1%–8% of the range. In addition, numerical analysis exhibited the limits of thermal and exergetic efficiency values possible to be obtained, when the boundary conditions are strongly controlled.

1. Introduction

High temperature heat exchangers, classified in the literature as those working above 500 [°C] [1], are key components in many technological and power generation systems. They are present in systems with a high temperature nuclear reactor or with fuel cells [2], petrochemical processes, or power units based on the Brayton cycle, including those using transcritical carbon dioxide [3].

Systems with an external combustion chambers are based on the gas cycles and form a new group of gas micro-CHP units. This solution is very promising for both prosumer and distributed power generation [4], in particular when units are powered with biofuels [5]. In such systems, there are two main important aspects for consideration – the first one connected with an increase in the efficiency, the second one with the small size of the system. A significant increase in microturbine efficiency can only be achieved by an increase in the engine operating temperature. Therefore, one of the critical elements in such installations is the recuperator (sometimes called a regenerative heat exchanger (RHX)), which contributes to the overall microturbine efficiency in a considerable proportion. Taking into account the system size and its efficiency, only compact heat exchangers with passive techniques of heat transfer intensification can fulfil strict requirements.

In literature, the plate and shell-and-tube heat exchangers are described as the most common units for high temperature applications. Regarding the plate heat exchangers, several variants of construction exist, but very often either a classical chevron-type or plate-fin are mentioned, as they are predominantly applied in industry [1] and considered in recuperative microturbine systems. For this application, Aquaro and Pieve [6] have pointed out the need of minichannel plate-fin or printed circuit heat exchangers development. An experimental analysis of a high temperature plate-fin heat exchanger was published by Haunstetter et al. [7]. Plates

were sintered and formed a gas-thight monolithic block, operated with air at temperature up to 800 [°C] and at the absolute pressure of up to 500 [kPa]. Thermal efficiency varied from 0.65 to 0.97. While results are promising, it was concluded that further research is necessary regarding the friction factor, since the pressure drop was relatively high − ranging from 2 [kPa] to 10 [kPa]. Considering the shell-and-tube heat exchangers [3], they are also widely used, but characterized by lower compactness, describing the ratio of the heat transfer area to the fluid volume. In the modern construction of heat exchangers, the most interesting are microchannel heat exchangers, with the hydraulic diameter of channels below 200 [μm] [8]. Compactness of such models can be higher than 10,000 [m^2/m^3] [9], and they require advanced and costly manufacturing techniques such as metal laser sintering, selective laser melting, or photochemical etching for the manufacturing of metal plates which are then welded using the diffusion method. A proposal of a novel, industrial-scale, high temperature heat exchanger was presented in [10]. The novelty arises from the utilization of hybrid heat transfer enhancement technologies (various insert types) to improve waste heat recovery efficiency. Performance optimization was conducted with the utilization of numerical algorithms validated with experimental data coming from investigations conducted at a temperature equal to 800 [°C] and at the pressure equal to 100 [kPa]. The optimized unit was characterized by the higher efficiency and the lower pressure drop.

It should be mentioned that numerical studies of the entire 3D heat exchanger geometry remain a computational challenge. In the literature, some examples referring to the classical plate heat exchanger [11] or to the compact heat exchanger [12] can be found. None of these examples was compared with the experimental data or referred to the minichannels type. An interesting analysis was presented in [13], where experimental and numerical studies of microchannel plate heat exchanger were reported. The shortage of such numerical analysis comes from the prevalent consideration of the 2D geometry of 1 plate, usually related to hydraulic performance. A numerical analysis of a simplified heat exchanger unit with various corrugation angles was also presented by Saha and Khan [14] who have utilized the k-ω SST turbulence model. Analyses were conducted in a wide range of both the Reynolds number values and temperature ranges, however this unit cannot be considered as a high temperature one. Numerical results correspond to the experimental ones within the range of 15−20% of discrepancy. The result of these analyses was a proposal for the general correlation of Nusselt number. A heat transfer correlation developed numerically was also proposed by de la Torre et al. [15]. It was formulated for a printed circuit heat exchanger which could be applied in the High Temperature Gas Cooled Reactor (HTGR). The authors analyzed a zigzag channel unit contributing to an increase of pressure drop, but at the same time resulting in a higher heat

transfer. The proposed Nusselt number correlation achieved a good agreement with the experimental data, however some numerical results differed from the experimental ones by up to 40%. A numerical simulation of the air heating by the recovery waste heat from a radiating exhaust gas flow in a plate heat exchanger was presented by Nia et al. [16]. The analysis considered the 2D laminar flow of media separated by the heat transfer surface. It was concluded that at analyzed conditions the radiation has a major influence on the heat transfer process. They have achieved the agreement between numerical and experimental results at the level of 12%.

The research regarding methods of heat transfer intensification causing better performance of heat exchangers for micro-CHP technologies has been conducted by present authors for many years. It refers to the classical plate [17], minichannel [18] and shell-and-tube heat exchangers with minichannels [19]. In the past, they were designed and tested in the domestic ORC unit. In this paper, a novel construction of plate minichannel heat exchanger, proposed for high-efficiency gas microturbine engines with an external combustion chamber, was considered.

As aforementioned, literature of the subject lacks investigations referring to a heat exchanger operating at temperature values above 900 [°C]. Despite the interest in such units, few studies have considered the numerical analysis of heat transfer and pressure drop in a simplified geometry (2D, few plates). Therefore, numerical analysis was involved in the investigation process. The Open-FOAM [20] software was used to construct the model of the transport processes occurring in the proposed heat exchanger and solve the equations. It should be emphasized that this software is rarely applied in simulations of such scale (a whole unit with all plates and channels). Boundary conditions were assumed on the basis of the experimental analysis. Numerical results helped to understand the pressure field and mass flow rate distribution in parallel with the temperature field in fluid and solid parts of the heat exchanger. The averaged numerical and experimental results obtained at the inlets and outlets were compared and provided a satisfactory agreement. Additionally, they were the basis for the determination of performance and led to the suggestions of its improvement through construction modifications.

2. Experimental analysis

The purpose of the experimental analysis was to check the prototype plate minichannel heat exchanger, and its hydraulic and thermal performance. The hydraulic performance was investigated at constant low-temperature conditions (called „cold" conditions), while the thermal one at high-temperature conditions (called „normal" operating conditions). An additional aim of such studies was to get the necessary data for setting boundary conditions in the
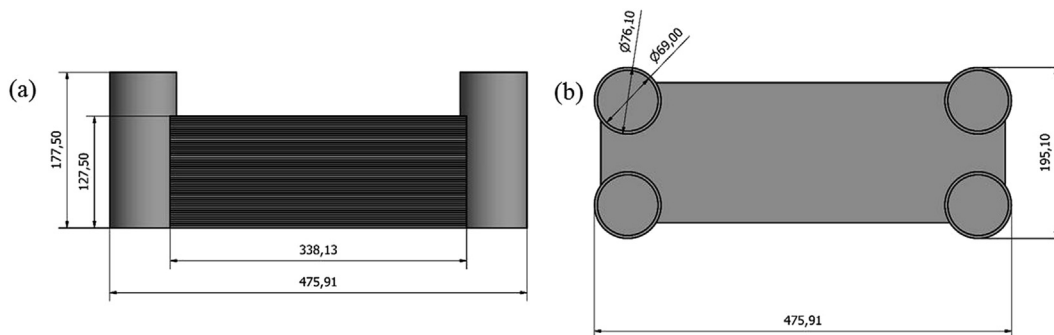

Fig. 1. Schematic view of plate minichannel heat exchanger, all dimensions are in [mm], (a) view from the side; (b) view from the top.

Table 1
Dimensions of the analyzed heat exchanger.

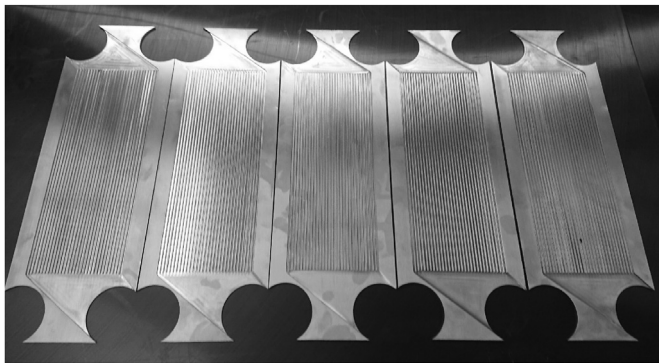| Dimensions	Value	Unit
Overall/working length	475.91/338.13	[mm]
Overall/working height	177.50/127.50	[mm]
Overall/working width	195.10/160.00	[mm]
Channel width/depth	3.00/1.50	[mm]
Inner diameter of inlets/outlets	69.00	[mm]
Outer diameter of inlets/outlets	76.10	[mm]
Number of plates hot/cold sides	25/25	–

Fig. 2. Photography of the plates and minichannels.

numerical analysis and then to compare the results. The air was chosen as the working fluid on both sides of the heat exchanger.

A schematic view of the prototype plate minichannel heat exchanger is shown in Figs. 1(a) and 1(b). It consists of 25 welded steel plates on the hot and cold sides, which were also welded to the headers. The plates were made with a CNC milling machine. Some of its dimensions are marked on Fig. 1, while all are listed in Table 1. In Fig. 2, the photography of the plates is shown, where the minichannels are clearly visible.

Experimental analysis was conducted at the Institute of Energy at Gdansk University of Technology. The schematic of operations of the facility is shown in Fig. 3(a), and a general view in Fig. 3(b). The main part of the stand was the prototype unit (1). It was connected to the combustion chamber (2), in which the gas burner (3) was located together with the heat exchanging coil (4). The exhaust gas outlet is marked as (5). The compressor (7) forced the flow of cold air, which mass flow rate was measured by the flowmeter (6) before entering the heat exchanger. The stand was equipped with the following devices for measurement of

- mass flow rate: Karman vortex flowmeter SITRANS FX330 by Siemens, measurement range 0.015−0.340 [kg/s], accuracy±1% for the air flow of 0.015−0.200 [kg/s] (in accordance with the certified calibration characteristics),
- temperature: thermocouple of *N*-type (TP-204N-1 b) by Czaki, measurement range up to 1250 [°C] and 1st class of accuracy,
- pressure difference: multifunctional measuring device TESTO 480 by Testo SE & Co, measuring range from −10 to +10 [kPa], resolution 0.0001 [kPa], accuracy ±0.0003 [kPa] +1% of the value measured in the range 0−2.5 [kPa].

Air was initially preheated in the heat exchanger (1). It then flowed through the heat exchanging coil, in which it was heated up to 957 [°C] by the exhaust gas. As the hot medium, it passed through the heat exchanger (1) on the hot side. Temperature of air was measured at inlets and outlets. Pressure drop was determined
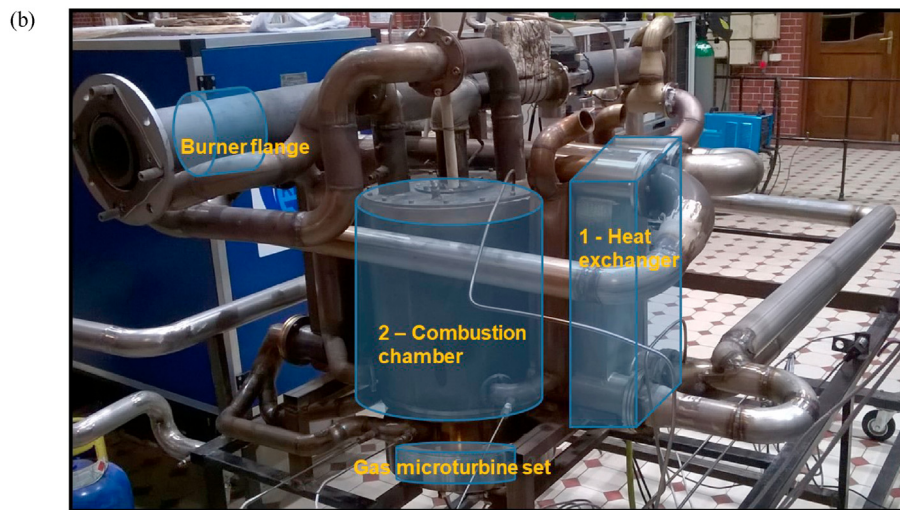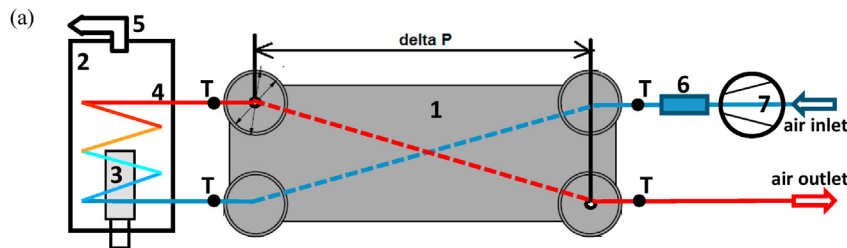

Fig. 3. (a) Representation of the experimental stand, 1 − heat exchanger, 2 − combustion chamber, 3 − gas burner, 4 − heat exchanging coil, 5 − exhaust gas outlet, 6 − flowmeter, 7 − compressor, (b) Real experimental setup, partial view.

between the inlet and outlet of the hot medium side, but during the „cold" conditions experiment. It was not examined during the „normal" operating conditions of the heat exchanger due to the problem with the pressure transducer. The heat rate was calculated from the following equation:

$$Q = \dot{m} c_p \Delta T \tag{1}$$

where Q is the overall heat rate, [W], $\dot{m}$ is the mass flow rate, [kg/s], c_p is the specific heat of the fluid, [J/(kg · K)] and ΔT is the temperature difference, [K].

The heat rate was specified at each side of the heat exchanger, namely, hot and cold, therefore the temperature difference represents the temperature difference between the inlet and outlet on a particular side. The results will be presented together with the results of numerical analysis.

3. Numerical model

3.1. Governing equations

Mathematical model was constructed on the basis of the following assumptions: stationary and non-compressible flow, Newtonian fluid, and 3D geometry. Density and other properties of the fluid have been assumed as temperature dependent. Processes of mass, momentum, and energy transfer fulfil the respective conservation laws and can be described by the following budget equations of mass (Equation (2)), momentum (Equation (3)), and energy (Equation (4)):

$$\frac{\partial \rho \overline{u_j}}{\partial x_j} = 0 \tag{2}$$

$$\frac{\partial}{\partial x_j} \left(\rho \overline{u_i u_j} \right) = -\frac{\partial \overline{p}}{\partial x_i} + \frac{\partial}{\partial x_j} \left(\rho \left(2\nu S_{ij} - \overline{u_i' u_j'} \right) \right) \tag{3}$$

$$\frac{\partial}{\partial x_j} \left(\overline{u_j} \Theta \right) = \frac{\partial}{\partial x_j} \left(a \frac{\partial \Theta}{\partial x_j} - \overline{u_j' \theta} \right) \tag{4}$$

where the velocity vectors are indexed as $u_{i,j}$, [m/s], ρ is fluid density, [kg/m^3], p - pressure, [Pa], ν - kinematic viscosity, [m^2/s], S_{ij} - the so-called strain rate tensor, [1/s], $\overline{u_i' u_j'}$ is turbulence related Reynolds stress tensor, [m^2/s^2], Θ - mean fluid temperature, [K], θ - its fluctuation, [K] which is used to define the $\overline{u_j' \theta}$ − turbulent heat flux, [K · m/s] and finally a is the fluid thermal diffusivity, [m^2/s].

Furthermore, Reynolds stress tensor is modelled with Equation (5):

$$-\overline{u_i' u_j'} = 2\nu_t S_{ij} \tag{5}$$

where ν_t is the turbulent viscosity, [m^2/s], modelled by a specific turbulence model to achieve the closure of the equation set. Turbulent heat flux is modelled in an analogical way and presented as Equation (6):

$$-\overline{u_j' \theta} = -\frac{\nu_t}{\sigma_t} \frac{\partial \Theta}{\partial x_j} \tag{6}$$

where σ_t is the turbulent Prandtl number.

The Reynolds stress tensor, precisely the turbulent viscosity, was modelled with the Realizable k-ε model (k indicates the turbulent kinetic energy, while ε − its dissipation). It was selected as the one, which can give good results, but does not require very fine mesh

near the wall due to the utilization of the wall functions. It is also characterised by the ability to predict the flow structure under strong adverse pressure gradients, recirculation, etc. As it will be shown further, such conditions occurred in the analyzed heat exchanger. This conclusion came from previous analysis of complex geometries and was confirmed by the literature report [21]. The Realizable k-ε model is modelled by two Equations, (7) and (8), as follows:

$$\frac{\partial}{\partial x_j} \left(\rho \overline{u_j} k \right) = \rho G - \rho \varepsilon - \frac{2}{3} \rho k \frac{\partial \overline{u_j}}{\partial x_j} + \frac{\partial}{\partial x_j} \left[\rho \left(\nu + \frac{\nu_t}{\sigma_k} \right) \frac{\partial k}{\partial x_j} \right] \tag{7}$$

$$\frac{\partial}{\partial x_j} \left(\rho \overline{u_j} \varepsilon \right) = C_1 \rho \sqrt{2 S_{ij} S_{ij}} \varepsilon - C_2 \rho \frac{\varepsilon^2}{k + \sqrt{\nu \varepsilon}} + \frac{\partial}{\partial x_j} \left[\rho \left(\nu + \frac{\nu_t}{\sigma_\varepsilon} \right) \frac{\partial \varepsilon}{\partial x_j} \right] \tag{8}$$

where G is the turbulence kinetic energy production, C_1, $C_2 = 1.9$, $\sigma_k = 1$, and $\sigma_\varepsilon = 1.2$ are model specific constants. The C_1 constant is defined as:

$$C_1 = \max \left[0.43, \frac{\eta}{\eta + 5} \right] \tag{9}$$

$$\eta = \sqrt{2 S_{ij} S_{ij}} \, \frac{k}{\varepsilon} \tag{10}$$

Heat transfer in the solid region was modelled using the following steady state formula for variable enthalpy h, considering
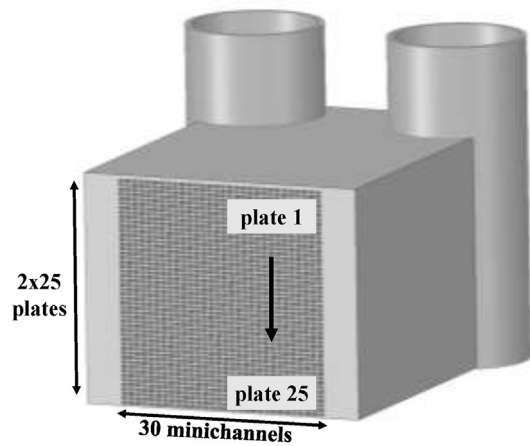

Fig. 4. Modelled geometry of heat exchanger. View of the heat exchanger crossection (considering both fluid sides). The way of plates numbering, shown schematically, will be used in the paper.
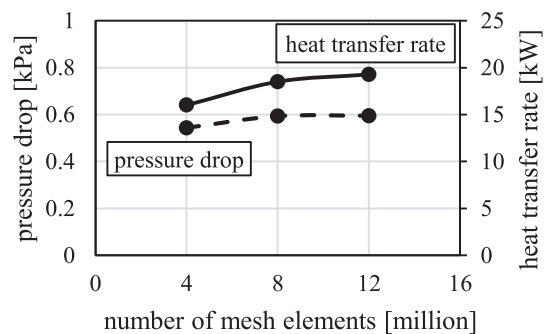

Fig. 5. Mesh independence test. The variables of interest were the pressure drop [kPa] on the hot side and the heat transfer rate [kW] between the cold and hot sides of the heat exchanger.

Table 2
Boundary conditions.

Parameter	Cold conditions	Normal conditions	
	Value		Unit
Mass flow rate of cold fluid	0.0252	0.0252	[kg/s]
Inlet temperature of cold fluid	18	31	[°C]
Mass flow rate of hot fluid	0.0252	0.0252	[kg/s]
Inlet temperature of hot fluid	18	957	[°C]
Outer wall heat flux	0	0	[W/m^2]
Reference pressure	100.6	100.6	[kPa]

Table 3
The results for the "cold" operation conditions.

Pressure drop	Cold side	Hot side	
	Value		Unit
Experimental analysis	0.6857	0.6073	[kPa]
Numerical analysis	0.5890	0.5950	[kPa]

temperature-dependent thermal conductivity κ, [W/(m · K)] and the specific heat c, [J/(kg·K)].

$$\frac{\partial}{\partial x_j}\left(\frac{\kappa}{c}\frac{\partial h}{\partial x_j}\right) = 0 \tag{11}$$

3.2. Geometry and boundary conditions

Model of geometry, reflecting the real geometry of the prototype unit, is presented in Fig. 4. Number of plates and channels together with the dimensions agreed with the prototype heat exchanger.

The next step of numerical model construction was related to the division of computational space and generation of the mesh. It was the most demanding task, due to large differences in a size of particular elements. A lot of problems have been met due to the number of minichannels. The base mesh size had a dimension of 1 mm. That value was reduced in the minichannels and near all other walls, to maintain a sufficient number of mesh nodes. The grid inside each minichannel consisted of approximately 4 × 4 nodes. The final mesh consisted of about 12 millions of elements, yet two others were also checked to identify convergence of the
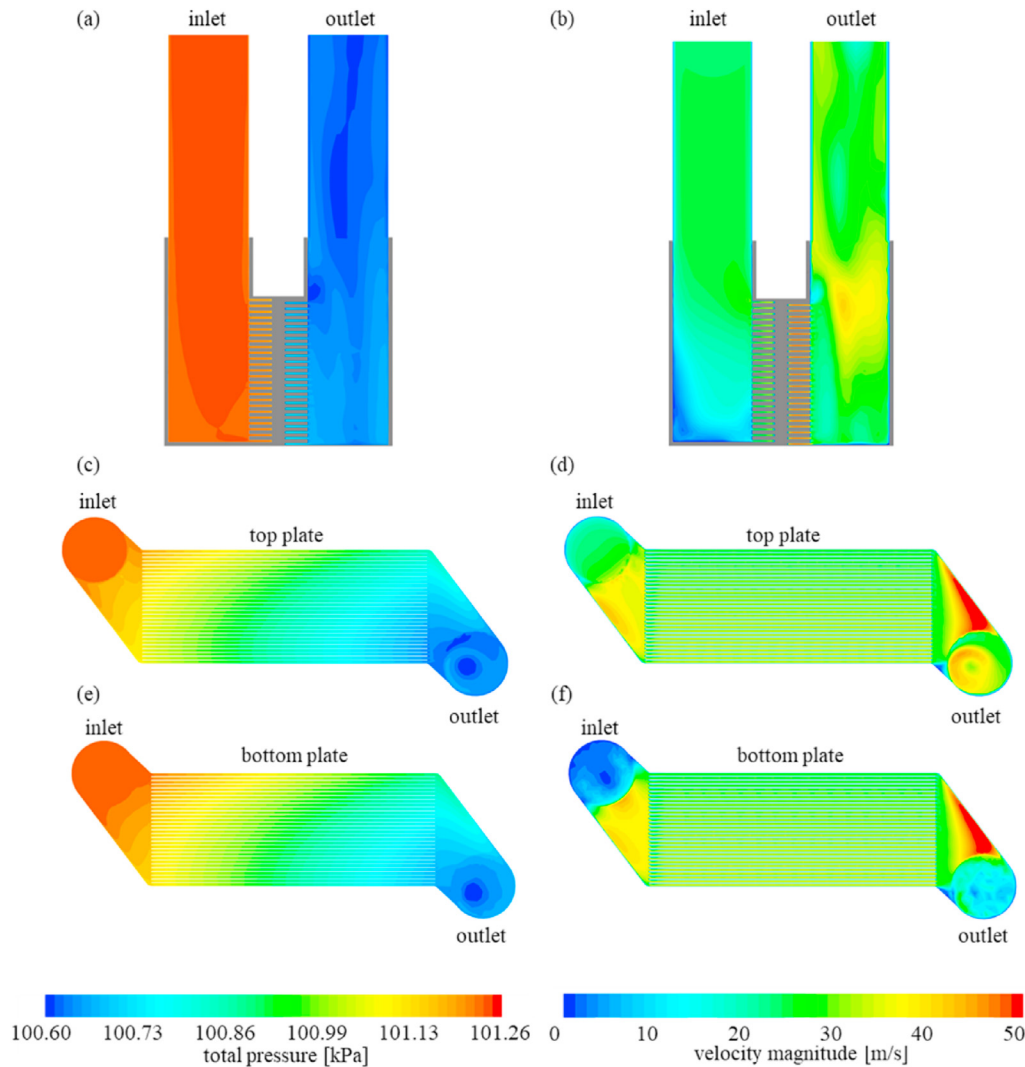

Fig. 6. (a), (c), (e): Pressure field and (b), (d), (f) velocity magnitude field in the case of "cold" operating conditions, in the inlet/outlet passages (a), (b) of the heat exchanger, in the minichannels of the top plate (c), (d) and in the bottom plate ones (e), (f).

solution: 4 and 8 million elements. It was constructed with polyhedral volumes inside the domain and single prismatic boundary layer elements on the fluid side. The main advantage of polyhedrals utilization was due to a reduction (by a factor of almost 3) of the initial tetrahedral elements number, as they were combined into polyhedral elements, which tend to be less skewed and less non-orthogonal. The mesh sensitivity studies, which were performed during the mesh generation process, were based on the controlling of two variables: the overall heat transfer rate between hot and cold fluids and the pressure drop of the hot side fluid flow between the inlet and outlet of the heat exchanger. They were monitored to determine the moment of calculation stabilization in relation to increased mesh elements and computational resources available. In Fig. 5, the results of the mesh studies are presented, referring to three mesh size values: 4, 8, and 12 million cells. As can be seen, the momentum stabilized faster than the heat transfer, which is often a problematic issue in CFD simulations, as the thermal analyses are more demanding in relation to the mesh quality. However, as the experimental results were available, the heat transfer results accuracy was also considered satisfying for the mesh of 12 million elements.

The OpenFOAM [20] environment was used to construct the model with the finite volume approach. The PLGrid Infrastructure was used to conduct the calculations. The segregated solver, *chtMultiRegionSimpleFoam* was used, and the final solution was obtained in an iterative manner. The procedure of numerical analysis was as follows:

- initialization of the fluid domains, solution variables, and boundary conditions,
- starting the SIMPLE loop for iteration *i*,
  - calculation of the momentum equation,
  - solution of the under-relaxed pressure equation,
  - correction of mass fluxes at all cell faces,
  - obtaining an improved velocity field,
  - calculation and under-relaxation of the energy equation of the fluid,
- initialization of the solid domain solution variables and boundary conditions,
- calculation and under-relaxation of the energy equation of the solid side,
- checking of convergence criteria, proceeding to iteration *i*+1 or finishing the process.

Numerical schemes of second-order upwind type were utilized, with additional limiting of the velocity gradient based on adjacent cell values. The pressure was calculated using the *geometric-algebraic multigrid* (GAMG) solver, and all other variables using the *stabilized preconditioned (bi-)conjugate gradient* (PBiCGStab) solver.

Applied boundary conditions, based on the experimental data, are listed in Table 2 for the cold and normal operation conditions. In the case of cold conditions, the constant properties of air were considered, while in the case of normal conditions the air was treated as the ideal gas with properties dependent on temperature.

4. Results

4.1. "Cold" operating conditions

Experimental and numerical analyses started with the case of cold operation conditions, it means the same flow conditions on both sides of the plate heat exchanger with minichannels. Air was at the same temperature of 18 [°C], with constant fluid properties. This part of the experiment was oriented on the hydraulic performance of the prototype unit. The results are presented in Table 3.

Good agreement between experimental and numerical results can be found. The results differed in the range of 2%–14%, while, for example, in [16] the discrepancy referring to the friction factor was in the range 11%–18% and treated as a very good one. Interesting is the discrepancy between cold and hot sides pressure drop in the case of experimental studies. Such a tendency was not exhibited by the results of numerical studies and was not expected, because both sides were identical geometrically and the properties of the working fluid were the same. Therefore, the conclusion, which came from these results, refers to some construction imperfections of the real prototype unit. It is hard to guess what kind of imperfection occurred there, but it can be supposed that some channels
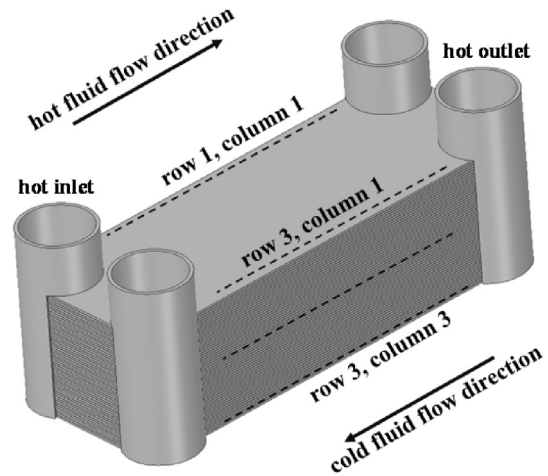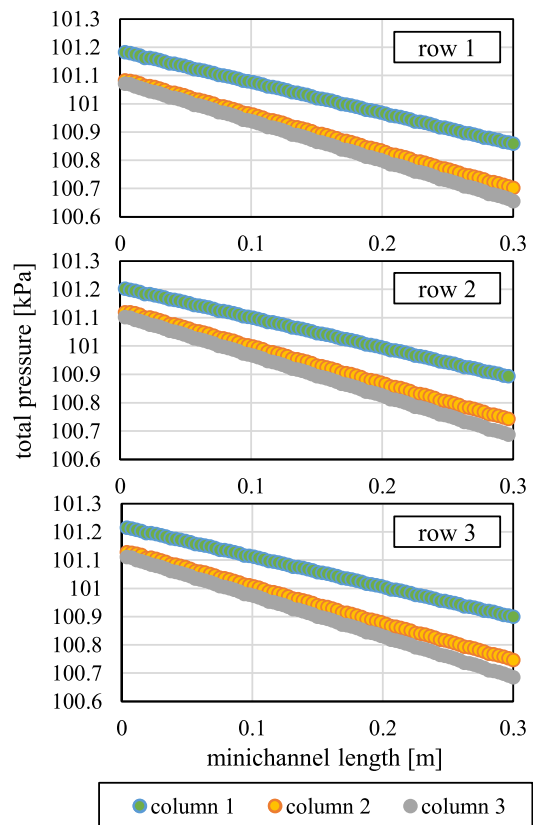
Fig. 7. Orientation of the plots in Fig. 8.

Fig. 8. Total pressure plots in selected minichannels, indicated schematically in Fig. 7.
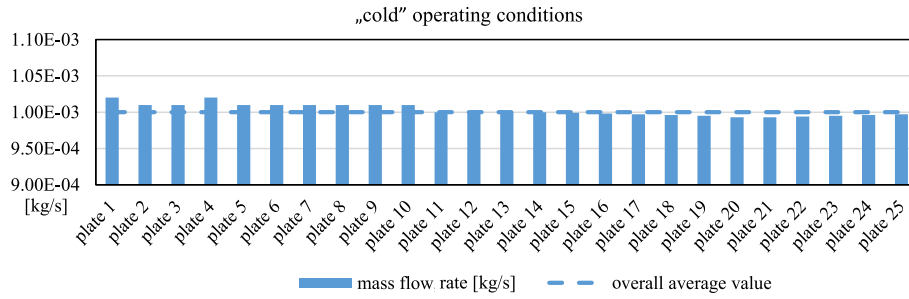
Fig. 9. Averaged mass flow rate through the minichannels of all heat exchanger plates (plate 1 represents the top while plate 25 the bottom one of the unit).

Table 4
The outlet temperature results for the "normal" operation conditions.

Outlet temperature	Cold medium	Hot medium	
	Value		Unit
Experimental analysis	692	240	[°C]
Numerical analysis	841	164	[°C]

could be partially or fully blocked. The differences between the numerical and experimental results could be also caused by factors such as manufacturing errors, entrance effect, roughness, and experimental uncertainties.

In Figs. 6(a), 6(c) and 6(e), the pressure distributions of the inlet and outlet parts of the heat exchanger are presented, as well as the cut planes through the first and the last plates. Please note that as
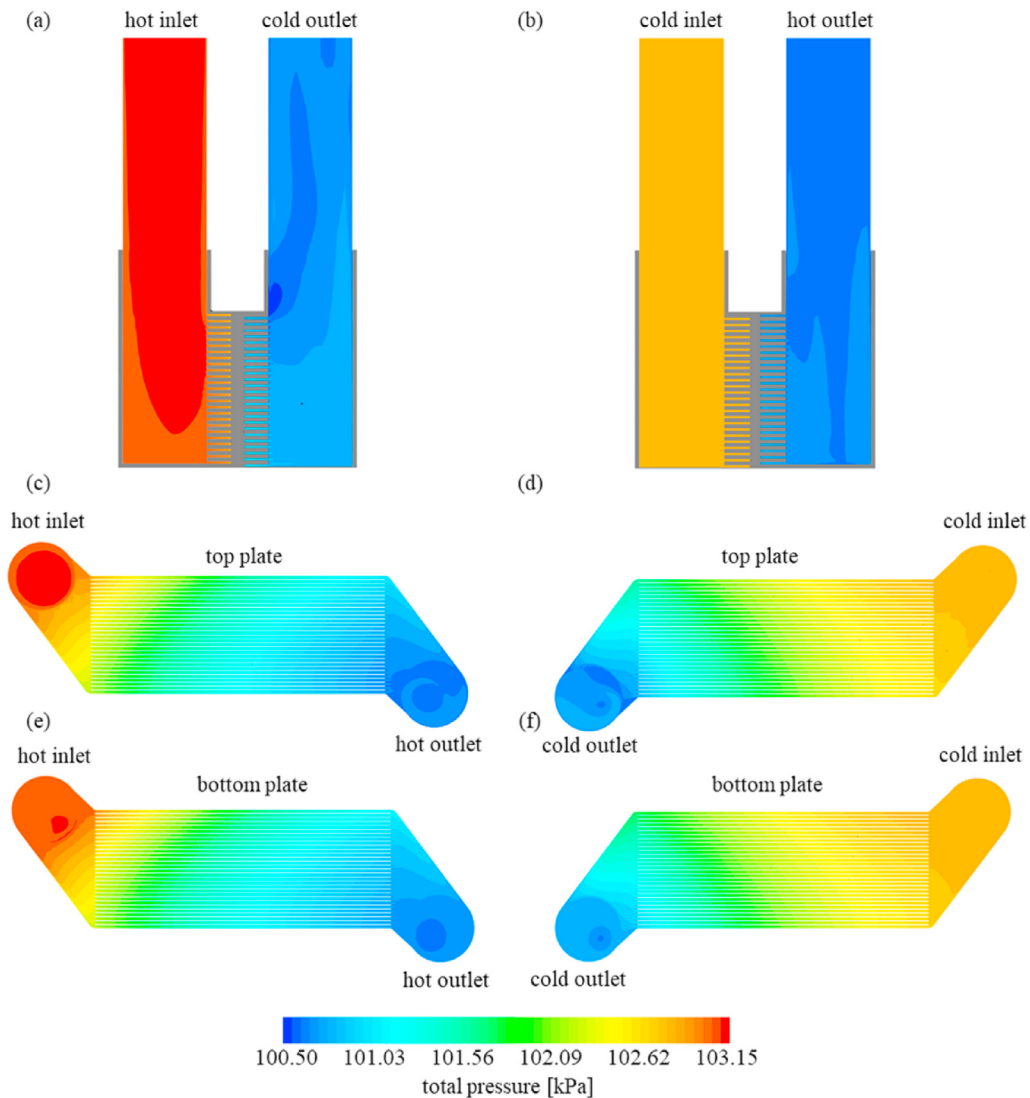

Fig. 10. Pressure field in the case of "normal" operation conditions (a), (b) in the inlet/outlet passages of the heat exchanger, minichannels of (c) top plate, hot side (e) bottom plate, hot side, (d) top plate, cold side (f) bottom plate, cold side.

the flow conditions and its characteristics were the same on the hot and cold side of the heat exchanger, just one inlet and one outlet are shown (two other areas are characterized by the same flow structures). Unequal pressure gradients in particular minichannels can be seen.

In Figs. 6(b), 6(d) and 6(f), the velocity magnitude distributions at the inlet and outlet parts of the heat exchanger are presented, as well as the cut planes through the first and the last plates. They correspond with the pressure fields in Figs. 6(a), 6(c) and 6(e). In the outlet region, the swirl, which is caused by the rapid acceleration of the flow leaving the minichannels, can be identified.

In Fig. 7 the relative orientation of the minichannels is shown, that would be used for the presentation of particular results. It is applied in Fig. 8, in which the pressure decrease along the 9 chosen channels is exhibited. Some differences are visible between the top and bottom locations, as well as the right and left sides of the heat exchanger, that extend the data presented in Fig. 6. Going further from the hot inlet to hot outlet (column 1 towards column 3), the local pressure loss increases from about 0.35 [kPa] to 0.4 [kPa].

In Fig. 9, the plot of the averaged mass flow rate values in particular plates from top to bottom is shown. It can be noticed that some differences occur and the highest flow rate values are found close to the upper part of the heat exchanger. This comes from the effect of choking at the heat exchanger bottom part and lower values of velocity. It was also shown in Fig. 6, where non-uniform velocity field is visible.

4.2. "Normal" operating conditions

Second stage of the analysis was connected with the case of normal operation conditions. The air temperature at the cold and hot inlets of the heat exchanger were 31 [°C] and 957 [°C], respectively. Comparison of the experimental and numerical results regarding the outlet temperature of cold and hot media is

presented in Table 4. The numerically obtained values were averaged over the outlet surface.

Considering thermal investigations of the prototype plate heat exchanger with minichannels the agreement between the outlet temperature values obtained experimentally and numerically is not satisfactory. The difference is in the range 22%−32%, however in [16] even 10%−40% of the discrepancy was presented as an acceptable result. There can be a few reasons of such discrepancy: firstly, some blockages in the minichannels, which could be also a basis for pressure drop value differences; secondly, the adiabatic boundary conditions, assumed at the outer heat exchanger surface, which should be changed into one taking into account some heat losses; thirdly: better numerical representation of inlet and outlet regions. All these reasons are a scope of further considerations.

4.2.1. Longitudinal distribution of parameters

Figs. 10 and 11 correspond to the results from Figs. 6 and 8. However, it was necessary to include and exhibit differences between cold and hot fluid flow. As indicated in Table 4, the temperature values between cold and hot sides were different, which resulted in various fluid properties along particular minichannels and different flow structures.

In Fig. 11, the pressure decrease along 9 channels is shown, in the same manner as in Fig. 8. The results are presented for the hot and cold fluid flows. The differences between the top and bottom locations, as well as the right and left sides of the heat exchanger are visible. This time, however, due to the temperature-dependent properties of the fluid, the pressure curves are different and not linear. The local pressure loss is higher than in the case of cold conditions and reaches the value of about 1 [kPa].

Figs. 12(a) and 12(b) present the velocity magnitude field in the inlets and outlets of hot and cold sides. It can be seen that the fluid speeds up when entering a narrow space of the collector before flowing to the minichannels, in which the velocity value gradually
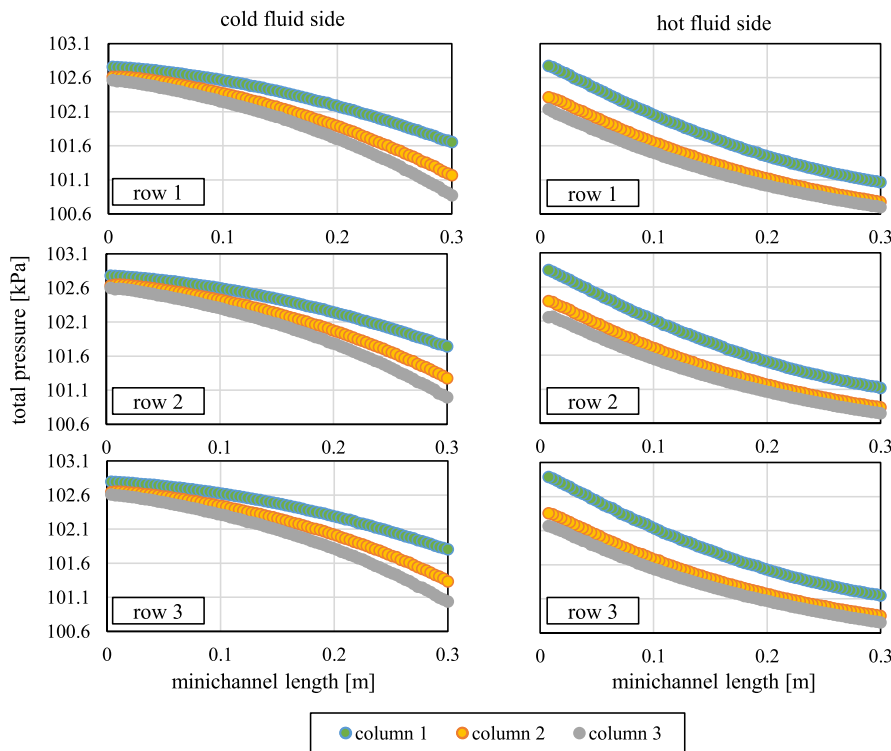

Fig. 11. Total pressure plots in the selected minichannels (indicated in Fig. 7), for both cold and hot fluid sides.

decreases. The outlet collector is divided into two regions, the first one just behind the minichannels with a low velocity, nearly rectangular and the second one, the triangular region of higher velocity values, which is located close to the wall. Region of low velocity values creates a kind of barrier, therefore in the outer region the fluid can move faster. In the outlet, the velocity contours look like spinning, what suggests tornado-like flow of the fluid. Fig. 12(c) represents the velocity field in the bottom plate of the hot side. The area of very low velocity can be seen, what looks like a recirculation zone. Velocity in the collector reaches very high values (about 40 [m/s]). In the minichannels, the velocity values decrease. The outlet region has similar velocity distribution like in Fig. 12(b). The velocity field in the top plate of the cold side is presented in Fig. 12(d). On the cold side the velocity values are increasing, what can be clearly visible by the colour changes of velocity contours. Outlet region also possesses similar features like in the case of the hot side (Figs. 12(b) and 12(c)), where the velocity values decrease at the outlets of minichannels and this region causes an increase of velocity values (up to 45 [m/s]) in the area close to the collector wall. In the outlet, the spinning velocity contours can be also found. It suggests the swirling flow in it. In Fig. 12(f), the velocity field in the

bottom plate of the cold side is shown. In the inlet, the velocity is characterised by a very low value, definitely it looks like stagnation or recirculation zone. It influences the velocity distribution inside the minichannels, where although the velocity value increases, a big part of the plate is characterised by low velocity values in comparison with Fig. 12(d). The velocity distribution in the outlet collector exhibits a similar tendency like in previous figures, it means the area of low velocity just behind the minichannels and a triangular area of higher velocity values. Very low velocity values can be found in the outlet.

4.2.2. Transverse distribution of parameters

Cross-sectional temperature field is presented in Fig. 13. Three planes were selected to show the temperature distribution in the fluid minichannels and in the solid construction material. The particular cross-sections are shown in Figs. 13(a), 13(b) and 13(c), respectively. Selected planes are schematically visualized above the results. In each subfigure, the temperature scale is different, because the temperature values vary in a wide range and the utilization of just one scale flattens a fine pattern of minichannels temperature. In Fig. 13(a), a big difference in temperature values
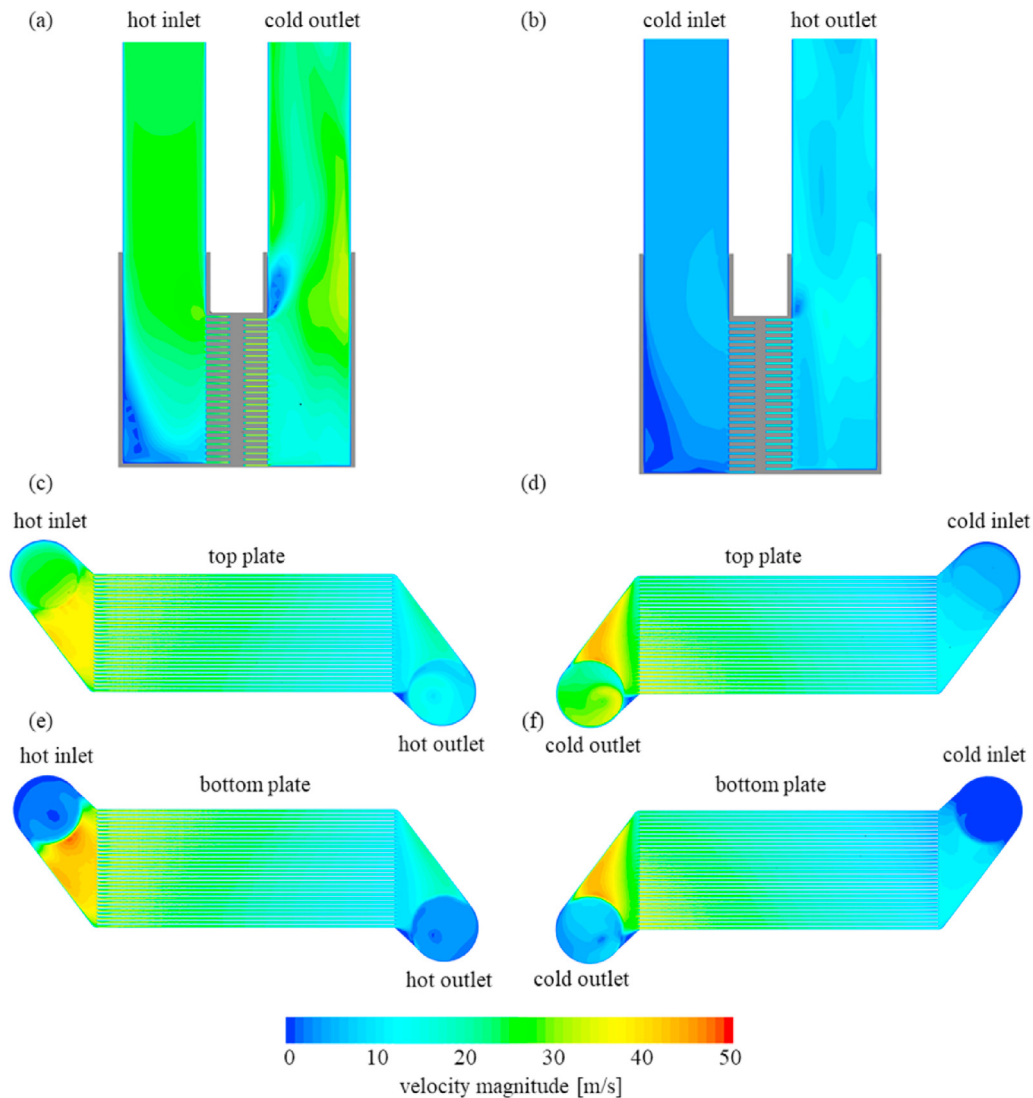

Fig. 12. Velocity magnitude field in the case of "normal" operation conditions (a), (b) in the inlet/outlet passages of the heat exchanger, minichannels of (c) top plate, hot side (e) bottom plate, hot side, (d) top plate, cold side (f) bottom plate, cold side.
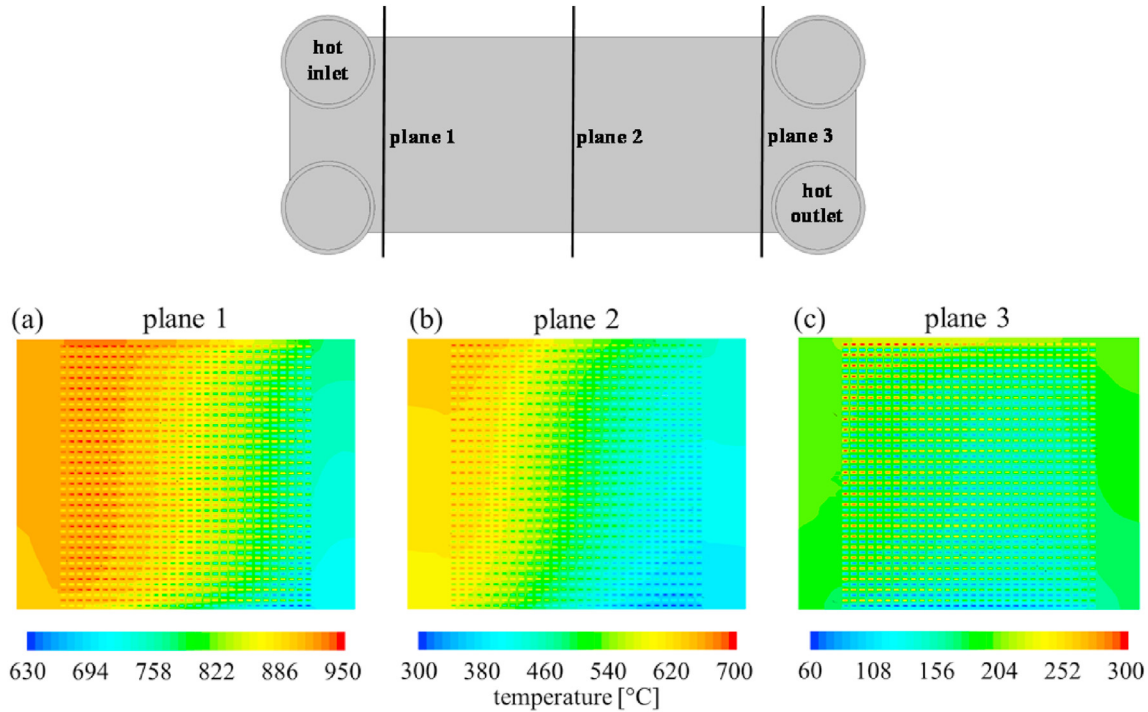
Fig. 13. Temperature field in the case of normal operation conditions in the heat exchanger cross-sections (a) plane 1, (b) plane 2, (c) plane 3.

within plane 1 can be observed. In plane 2 (Fig. 13(b)), the temperature field is divided in two nearly symmetrical parts. The axis of symmetry is diagonal. In Fig. 13(c), the temperature range is very narrow, what suggests very effective heat transfer.

Temperature distribution across the top plate on the hot (left column) and cold (right column) sides is presented in Fig. 14. Three planes were selected to show the temperature values of the wall and fluid. In Fig. 14(a), the results for plane 1 are presented. It should be pointed out that on the hot and cold sides, this line is located at the opposite ends of the plate. In Figs. 14(b) and 14(c), the results for planes 2 and 3 are shown, respectively. The results are shown in relation to the central axis of the plate minichannel heat exchanger unit, therefore the distance is in the range −0.06 [m] to 0.06 [m], what gives 0.12 [m] of the working area width. In the left column, the temperature values of the fluid are higher than the wall ones, while in the right column, the temperature values of the wall are higher than the fluid ones. Close to the inlet of the hot fluid, the temperature difference between the fluid and the wall is relatively low in the area close to −0.06 [m]. In the opposite side (close to 0.06 [m]), the temperature difference is larger. In the right column (cold side), the distribution of wall temperature is almost constant. Cold fluid temperature distribution exhibits some inclination, but is also nearly constant. The lowest temperature value could be found in the region close to the cold fluid inlet. Plane 2 temperature distribution (Fig. 14(b)) for both hot and cold sides represents a small temperature difference and what is more important, this difference is almost constant along the plate width. However, temperature values differ significantly in the regions close to −0.06 [m] or 0.06 [m]. Fig. 14(c) shows the results along plane 3. In the case of the hot side (left column), the temperature distribution is almost constant for the wall and nearly constant for the fluid. In the case of the cold side (right column), the temperature difference between the fluid and wall, close to the outlet (−0.06 [m]), takes lower values than on the other side of the plate (0.06 [m]).

In Figs. 15 and 16, another proof of differences between the fluid and adjacent wall temperature is shown. The order of all plots was indicated in Fig. 7. The temperature distribution is along three rows in two particular columns, 1 and 3. In Fig. 15, the temperature difference between the fluid and wall becomes more visible when going away from the hot fluid inlet. Temperature of fluid is higher than the wall and it can suggest some heat transfer lag, what might influence the performance of this process. In Fig. 16 the results for the cold side are presented. In this case, the temperature of the wall is higher than the fluid and the difference between them increases when going away from the cold fluid inlet. It is important to remember that the direction of flow is opposite in the plots in Figs. 15 and 16. That explains the different curvatures of the plots of cold and hot sides. The temperature field explains distribution of the mass flow rate, which is presented in Fig. 17.

4.2.3. Mass flow rate

In Fig. 17, the averaged mass flow rate distribution of the plates is presented, corresponding to the one in Fig. 9. In contrary to the "cold" conditions results, the mass flow rate values are characterized by different behaviour. The highest mass flow rate values occur at the bottom plates. It is related to the varying density, which impacts the mass flow values.

The most homogeneous distribution can be found in the middle part of the heat exchanger. The biggest deviation was in the range 5%−6.5% in the case of hot side and for the cold one from 3% to 5%.

4.2.4. Heat exchanger performance

Considering the thermal performance of the plate heat exchanger with minichannels, the experimentally obtained heat rate was determined on the basis of Equation (5), while the numerically obtained one was calculated as the average value over the wetted area. This area in the hot and cold sides was equal to 2.029 [m^2]. The results are presented in Table 5.

The cold side exhibits about 8% of discrepancy in comparison with the hot side, what can confirm the conclusion stemming from the analysis of pressure drop (Table 3) about some imperfections of heat exchanger manufacturing. On the hot side, the experimental
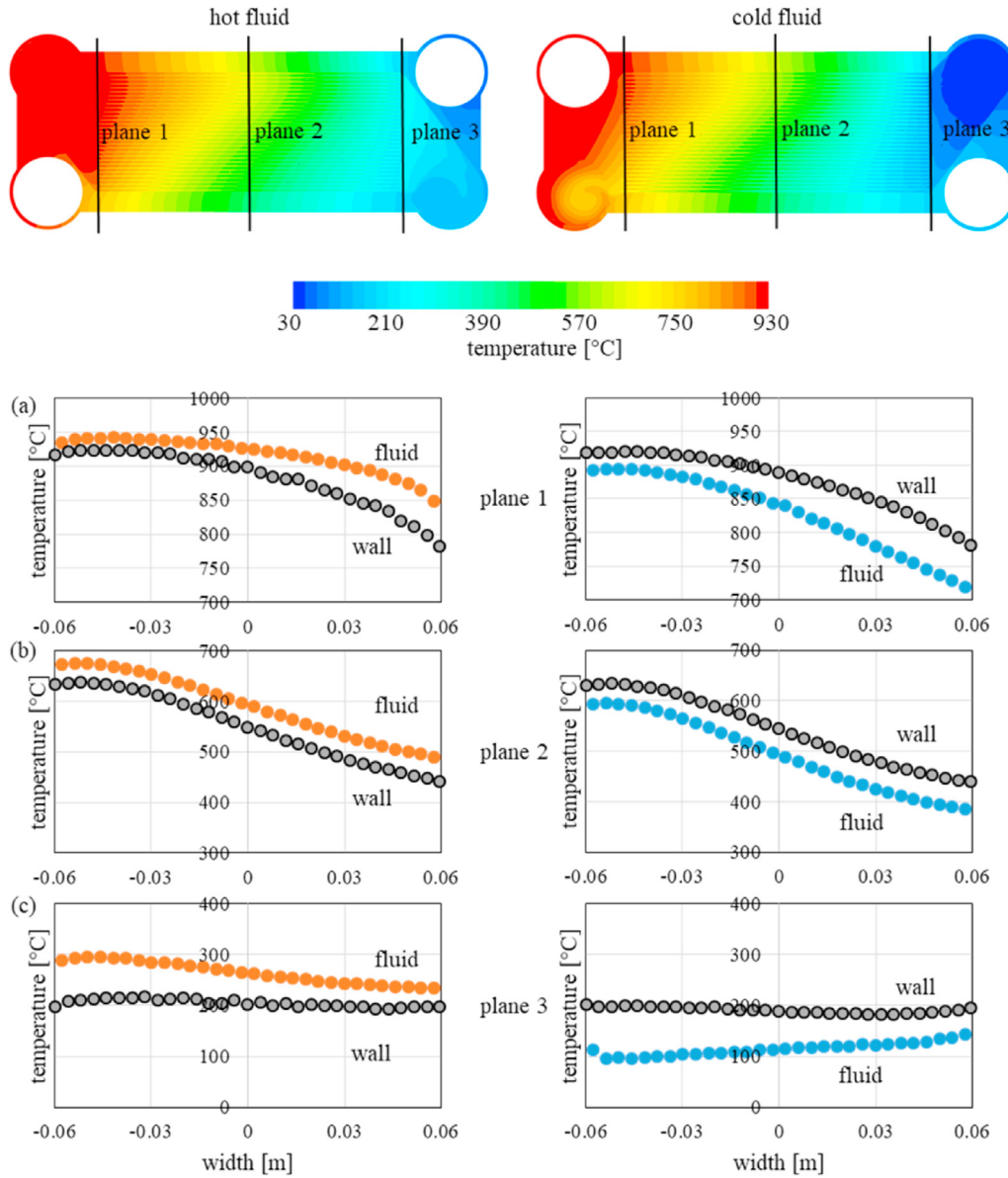
Fig. 14. Temperature distribution in the case of normal operation conditions in the top plate of the heat exchanger, hot side − left column, and cold side − right column at three selected cross-cut planes, (a) plane 1, (b) plane 2, (c) plane 3.

and numerical results agreed within 1%, while on the cold side were within 7%.

The performance of the heat exchanger can be evaluated on the basis of effectiveness η_t, defined as [22]:

$$\eta_t = \frac{\dot{m}_c(h_{out,c} - h_{in,c})}{\dot{m}_h h_{in,h} - \dot{m}_c h_{in,c}} \cdot 100\% \tag{12}$$

where $h_{in,c}$ is the inlet specific enthalpy of the cold fluid, $h_{out,c}$ is the outlet specific enthalpy of the cold fluid, and $h_{in,h}$ is the inlet specific enthalpy of the hot fluid.

Exergy efficiency η_x is defined for the adiabatic heat exchanger in agreement with the assumption done in the numerical analysis, in the following form [23]:

$$\eta_x = \frac{\dot{m}_c(x_{out,c} - x_{in,c})}{\dot{m}_h(x_{in,h} - x_{out,h})} \cdot 100\% \tag{13}$$

$$x_i = (h_i - h_0) - T_0(s_i - s_0) \tag{14}$$

where $\dot{m}_{c,h}$ are the mass flow rates of the cold and hot fluid, [kg/s], the dead state is defined by temperature T_0 equal to 25 [°C] and pressure 100 [kPa], $x_{in,out}$ are the inlet and outlet specific exergy [J/kg], and s_i represents the specific entropy [J/(kg·K)].

In the definition formulated in Equation (14), the changes of flow potential and kinetic energy changes have been neglected. In the calculations, no pressure losses have been assumed. The calorific parameters have been taken from Refprop v.9.0 [24]. The results are presented in Table 6.

Effectiveness of the analyzed prototype heat exchanger was equal to 69.6%, while the exergy one equalled to 66.8%. The values obtained from numerical analysis were slightly higher (86.6% and 85.9%, respectively). The reasons of the differences come from the previously discussed manufacturing process errors and the numerical boundary conditions applied at the outer wall of the heat exchanger.
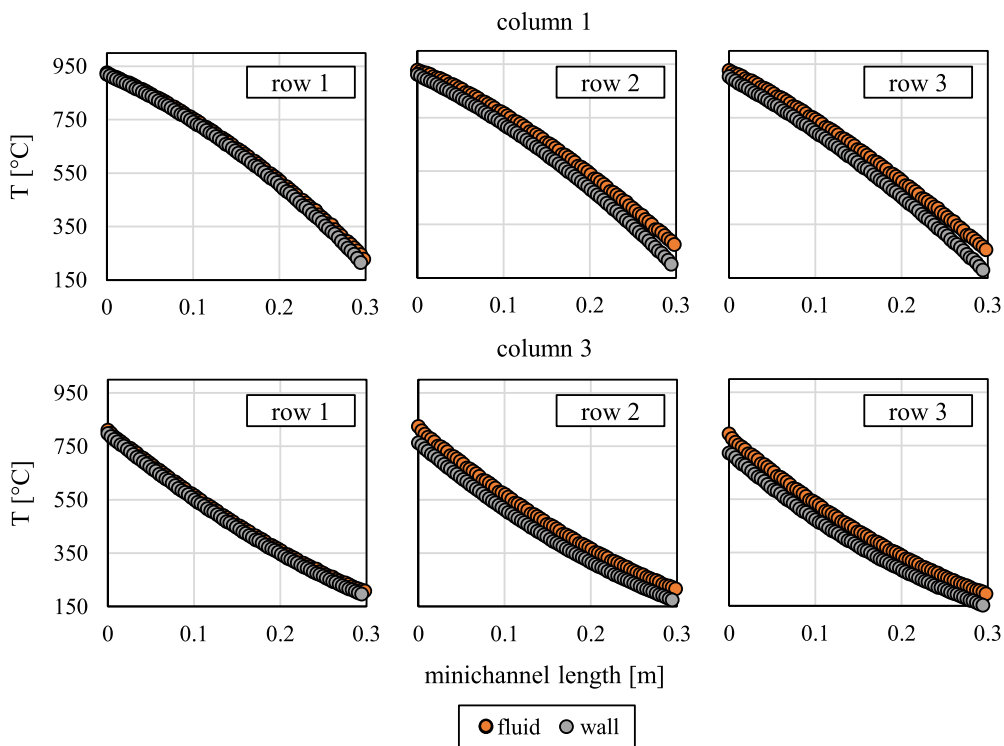
Fig. 15. Temperature along particular hot fluid minichannels. Orange colour indicates hot fluid, grey − wall. (For interpretation of the references to colour in this figure legend, the reader is referred to the Web version of this article.)
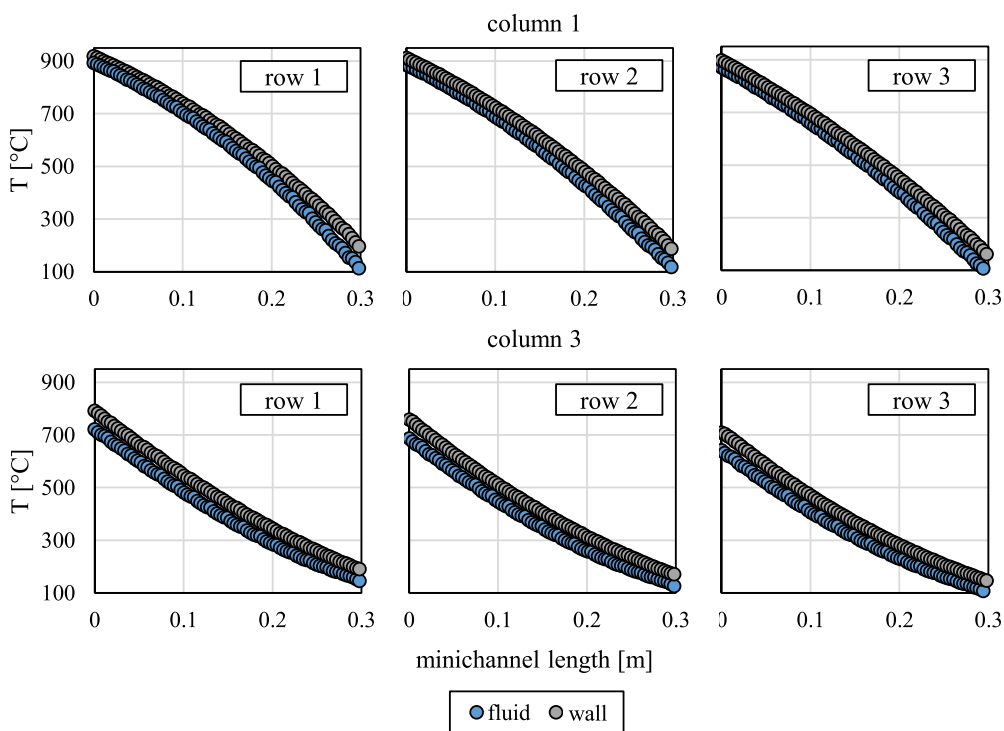
Fig. 16. Temperature along particular cold fluid minichannels. Blue colour indicates cold fluid, grey − wall. (For interpretation of the references to colour in this figure legend, the reader is referred to the Web version of this article.)
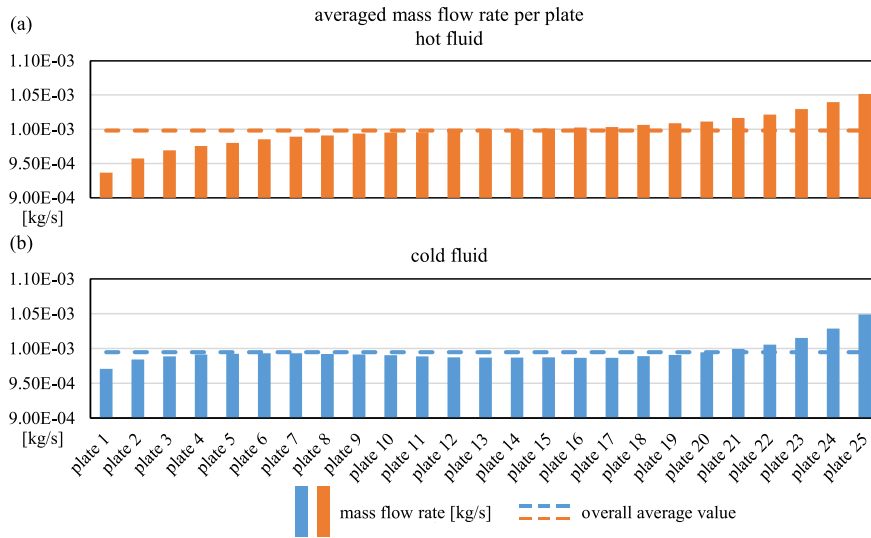
Fig. 17. Averaged mass flow rate through plates 1 (top) to 25 (bottom). (a) Hot fluid side (orange colour), (b) cold fluid side (blue colour). (For interpretation of the references to colour in this figure legend, the reader is referred to the Web version of this article.)

Table 5
Heat rate results for the "normal" operation conditions.

Heat rate	Cold medium	Hot medium	
	Value		Unit
Experimental analysis	18.000	19.500	[kW]
Numerical analysis	19.278	19.276	[kW]

Table 6
Effectiveness and exergy efficiency values.

Performance	η_t	η_x
Experimental analysis	69.6%	66.8%
Numerical analysis	86.6%	85.9%

5. Conclusions

The numerical analysis of the plate minichannel heat exchanger was conducted on the basis of boundary conditions coming from the experimental analysis. Considering the velocity field at the inlets on both sides of the plate minichannel heat exchanger, the recirculation or stagnation zones could be identified in the area close to the bottom plates. These zones influence the velocity distribution in the minichannels. Close to the top plates, also on both sides of the analyzed unit, the spinning velocity contours suggest tornado-like movement of the fluid. Considering the temperature, its distribution on the plates of the hot and cold sides exhibits inequalities along and across the plates. The middle part of the heat exchanger unit is characterized by the constant temperature difference between the fluid and the wall on both sides. Presented temperature fields, varying in space, suggest heat transfer not only through the wall, but also along it, therefore the phenomena of axial conduction [25] should be taken into account.

Satisfactory agreement between the experimental and numerical results was obtained, however some discrepancies were also found. They were mainly related to the fluid temperature values at the outlet, cold side, pressure drop, and heat rate. The experimental and numerical results, regarding the outlets temperature values agreed within the 22%−32% range, the pressure drop agreed within the 2%−14% range, while the heat rate − within the 1%−7% range.

Referring to the outlet values of fluid temperature, few issues, which could contribute to the discrepancies were pointed out, namely, the nonideal construction of the heat exchanger unit and adiabatic boundary conditions assumed at the outer heat exchanger surface. Regarding the cold side pressure drop and heat transfer rate, the results suggest again some problems with the manufacturing or assembly of the heat exchanger. Analysis of local thermal and hydraulic results, it was a source of findings (stagnation, recirculation zone of the fluid, or axial conduction), which can help to improve the construction of plate minichannel heat exchanger and to optimize its performance.

Declaration of competing interest

The authors declare that they have no known competing financial interests or personal relationships that could have appeared to influence the work reported in this paper.

Nomenclature

a	thermal diffusivity, $[\text{m}^2/\text{s}]$
c	specific heat, $[\text{J}/(\text{kg} \cdot \text{K})]$
C_1	Realizable k-ε model constant, $-$
C_2	Realizable k-ε model constant, $-$
G	turbulent kinetic energy production, $[\text{m}^2/\text{s}^2]$
h	specific enthalpy, $[\text{J}/\text{kg}]$
k	turbulent kinetic energy, $[\text{m}^2/\text{s}^2]$
κ	thermal conductivity, $[\text{W}/(\text{m} \cdot \text{K})]$
$\dot{m}$	mass rate, $[\text{kg}/\text{s}]$
$\overline{p}$	average pressure, $[\text{Pa}]$
Q	heat rate, $[\text{W}]$
s	specific entropy, $[\text{J}/(\text{kg}\cdot\text{K})]$
S_{ij}	strain rate tensor, $[1/\text{s}]$
T	temperature, $[\text{K}]$
$\overline{u_{i,j}}$	average velocity component, $[\text{m}/\text{s}]$
$\overline{u'_i u'_j}$	Reynolds stress tensor, $[\text{m}^2/\text{s}^2]$
$\overline{u'_j \theta}$	turbulent heat flux, $[\text{K} \cdot \text{m}/\text{s}]$
ε	turbulent kinetic energy dissipation, $[\text{m}^2/\text{s}^3]$
η_t	effectiveness
η_x	exergy efficiency
Θ	average temperature, $[\text{K}]$
θ	temperature fluctuation, $[\text{K}]$
ν	kinematic viscosity, $[\text{m}^2/\text{s}]$
ν_t	turbulent viscosity, $[\text{m}^2/\text{s}]$
ρ	density, $[\text{kg}/\text{m}^3]$
σ_k	Realizable k-ε model constant
σ_t	turbulent Prandtl number
σ_ε	Realizable k-ε model constant

Indexes

c	cold
h	hot
i	representative point of the heat exchanger's inlet or outlet
in	inlet
out	outlet
0	dead state

References

[1] Zhang X, Keramati H, Arie M, Singer F, Tiwari R, Shooshtari A, Ohadi M. Recent developments in high temperature heat exchangers: a review. Frontiers in Heat and Mass Transfer 2018;11:18.

[2] Kwaśniewski T, Piwowarski M. Design analysis of hybrid gas turbine fuel cell power plant in stationary and marine applications. Pol Marit Res 2020;27(2): 107−19.

[3] Chordia L. High temperature heat exchanger design and fabrication for systems with large pressure differentials. Final Scientific/Technical Report; 2017. https://www.osti.gov/biblio/1349235. [Accessed 19 April 2020].

[4] Kosowski K, Tucki K, Piwowarski M, Stępień R, Orynycz O, Włodarski W. Thermodynamic cycle concepts for high-efficiency power plants. Part B: prosumer and distributed power industry. Sustainability 2019;11:2647.

[5] Mikielewicz D, Kosowski K, Tucki K, Piwowarski M, Stępień R, Orynycz O, Włodarski W. Gas turbine cycle with external combustion chamber for prosumer and distributed energy systems. Energies 2019;12(18):3501.

[6] Aquaro D, Pieve M. High temperature compact heat exchangers: performance of advanced metallic recuperators for power plants. In: Proc. Of Fifth International Conference on enhanced, compact and Ultra-compact heat exchangers: Science, engineering and Technology; 2005. https://core.ac.uk/download/pdf/185670699.pdf. [Accessed 10 February 2021].

[7] Haunstetter J, Dreißigacker V, Zunft S. Ceramic high temperature plate fin heat exchanger: experimental investigation under high temperatures and pressures. Appl Therm Eng 2019;151:364−72.

[8] Kandlikar SG, Grande WJ. Evolution of microchannel flow passages - thermohydraulic performance and fabrication technology. Heat Tran Eng 2003;24(1):3−17.

[9] Kreith F. Heat and mass transfer. Mechanical engineering handbook. CRC Press LLC; 1999.

[10] Zhang P, Ma T, Li W-D, Ma G-Y, Wang Q-W. Design and optimization of a novel high temperature heat exchanger for waste heat cascade recovery from exhaust flue gases. Energy 2018;160:3−18.

[11] Żukowski W, Migas P, Gwadera M, Larwa B, Kandafer S. A numerical analysis of heat transfer in a crosscurrent heat exchanger with controlled and newly designed air flows. Open Chemistry 2018;16:627−36.

[12] Kan M, Ipek O, Gurel B. Plate heat exchangers as a compact design and optimization of different channel angles. Acta Phys Pol, A 2015;128:49−52.

[13] Yang Y, Brandner JJ, Morini GL. Hydraulic and thermal design of a gas microchannel heat exchanger. J Phys Conf 2012;362:012023.

[14] Saha SK, Khan AH. Numerical study on the effect of corrugation angle on thermal performance of cross corrugated plate heat exchangers. Thermal Science and Engineering Progress 2020;20:100711.

[15] de la Torre R, François J-L, Lin C-X. Optimization and heat transfer correlations development of zigzag channel printed circuit heat exchangers with helium fluids at high temperature. Int J Therm Sci 2021;160:106645.

[16] Nia MF, Nassab SAG, Ansari AB. Numerical simulation of air heating by the recovered waste heat from the radiating exhaust gas flows in a plate heat exchanger. Int J Therm Sci 2021;161:106728.

[17] Wajs J, Mikielewicz D. Effect of surface roughness on thermal-hydraulic characteristics of plate heat exchanger. Key Eng Mater 2014;597:63−74.

[18] Wajs J, Mikielewicz D, Fornalik-Wajs E. Thermal performance of a prototype plate heat exchanger with minichannels under boiling conditions. J Phys Conf 2016;745:032063.

[19] Wajs J, Mikielewicz D, Jakubowska B. Performance of the domestic micro ORC equipped with the shell-and-tube condenser with minichannels. Energy 2018;157:853−61.

[20] OpenFOAM Extended code guide − Available at: https://www.openfoam.com/documentation/guides/latest/doc/[Accessed 18.02.2021].

[21] Zuckerman N, Lior N. Jet impingement heat transfer: physics, correlations, and numerical Modeling. Adv Heat Tran 2006;39:565−631.

[22] Pn-En 308. Heat exchangers. Test procedures for establishing the performance of air to air and flue gases heat recovery devices. Warszawa: Polish Committee for Standardization; 2001. 2001.

[23] Alimoradi A. Investigation of exergy efficiency in shell and helically coiled tube heat exchangers. Case Studies in Thermal Engineering 2017;10:1−8.

[24] National Institute of standards (NIST). Refprop v 2010;9.

[25] Maranzana G, Perry I, Maillet D. Mini- and micro-channels: influence of axial conduction in the walls. Int. J. Heat Mass Transf. 2004;47:3993−4004.